Icarus xxx (2013) xxx–xxx

Contents lists available at ScienceDirect

Icarus

journal homepage: www.elsevier.com/locate/icarus

The Vesta gravity field, spin pole and rotation period, landmark positions, and ephemeris from the Dawn tracking and optical data

A.S. Konopliv [a,*], S.W. Asmar [a], R.S. Park [a], B.G. Bills [a], F. Centinello [b], A.B. Chamberlin [a], A. Ermakov [b], R.W. Gaskell [c], N. Rambaux [d,e], C.A. Raymond [a], C.T. Russell [f], D.E. Smith [g], P. Tricarico [c], M.T. Zuber [b]

[a] Jet Propulsion Laboratory, California Institute of Technology, Pasadena, CA 91109, USA
[b] Massachusetts Institute of Technology, Cambridge, MA 02139-4307, USA
[c] Planetary Science Institute, Tucson, AZ 85719, USA
[d] Universiťe Pierre et Marie Curie, UPMC 06, Paris, France
[e] IMCCE, Observatoire de Paris, CNRS UMR 8028, 77 Avenue Denfert-Rochereau, 75014 Paris, France
[f] Institute of Geophysics and Planetary Physics, University of California, Los Angeles, CA 90095-1567, USA
[g] Solar System Exploration Division, NASA Goddard Space Flight Center, Greenbelt, MD 20771, USA

ARTICLE INFO

Article history:
Available online xxxx

Keywords:
Asteroid Vesta
Asteroids, dynamics
Asteroids, rotation
Geophysics

ABSTRACT

The Vesta gravity field and related physical parameters have been precisely measured using 10-months of radiometric Doppler and range data and optical landmark tracking from the Dawn spacecraft. The gravity field, orientation parameters, landmark locations, and Vesta's orbit are jointly estimated. The resulting spherical harmonic gravity field has a half-wavelength resolution of 42 km (degree 20). The gravitational mass uncertainty is nearly 1 part in 10^6. The inertial spin pole location is determined to better than 0.0001° and the uncertainty in the rotation period has been reduced by nearly a factor of 100. The combined precession and nutation of the pole of Vesta has been detected with angular rates about 70% of expected values, but not well enough to constrain the moment of inertia. The optical landmark position estimates reduce the uncertainty in the center-of-mass and center-of-figure offset to 10 m. The Vesta ephemeris uncertainty during the Dawn stay was reduced from 20 km to better than 10 m in the Earth–Vesta direction.

1. Introduction and background

The gravity field of Vesta together with the image-derived shape model (Raymond et al., 2011; Jaumann et al., 2012) allows one to constrain models of the interior structure from the crust to the core (Zuber et al., 2011) of the next most massive proto-planet in the asteroid belt after Ceres. The gravity field is mainly derived from the shape and is fairly homogeneous with no mascons evident (e.g. similar to those on the Earth's Moon or Mars, e.g. Muller and Sjogren, 1968). The multi-layer interior models best match the observed gravity for crustal densities with limited porosity (~10% or crustal densities of 3.0 g/cm^3, Ermakov et al., 2013; Park et al., 2013). Although there is a strong correlation between gravity and topography indicating a fairly uniform density for Vesta, changes in internal structure are evident in multiple features (e.g., the Rheasilvia impact basin), and with more mass variation in the north–south direction versus the east–west direction (Bills et al., 2013). Comparing the observed second degree harmonic J_2 (related to the flattening) in the gravity field to that of a gravity field derived from a homogeneous shape, the oblateness is consistent with a probable core (Russell et al., 2012). Although the probable core size and density are not independently determined, for an assumed core density between 7.1 and 7.8 g/cm^3 based upon iron meteorites and considering a range of core flattening, the core size is in the range 107–113-km (Russell et al., 2012) for a mantle and core model (no crust) with each layer homogeneous. Alternate homogeneous layered crust and mantle only models (no core) with a ~50-km 3.0 g/cm^3 crust and a 3.9 g/cm^3 mantle with 0.1 flattening also match the observed J_2, but this crustal thickness is in excess of the upper limit of estimates based on Dawn observations and HED compositions (30–41 km, Mandler and Elkins-Tanton, 2013; >19-km, McSween et al., 2011; 15–20 km, McSween et al., 2013; 24–42 km eucritic crust, Ruzicka et al., 1997).

The irregular shape of Vesta consequently implies a very irregular gravity field. This presents challenges for the mission design due to large orbit perturbations caused by the gravity field (~50 km for the low altitude orbits due to a 12 days long period variation in eccentricity) and performing low thrust solar electric propulsion (SEP) orbit transfers through resonance with the rotation period of Vesta (Tricarico and Sykes, 2010; Delsate, 2012). The Dawn SEP mission with large solar arrays (about double the

* Corresponding author.
E-mail address: alex.konopliv@jpl.nasa.gov (A.S. Konopliv).

0019-1035/$ - see front matter © 2013 Elsevier Inc. All rights reserved.
http://dx.doi.org/10.1016/j.icarus.2013.09.005

surface area of other typical gravity missions such as MGS or MRO), imply larger non-gravitational force models. Also, another challenge to the gravity investigation is that the spherical harmonic representation of the gravity field cannot be mapped to the entire surface of Vesta.

The spherical harmonics are known to converge outside the smallest sphere that encloses Vesta (e.g. the Brillouin sphere of ~293-km, Grafarend and Engels, 1994; Heiskanen and Moritz, 1967). However, for practical purposes, the spherical harmonics converge to all locations outside a 290 × 265-km ellipsoid that is smaller than the Brillouin sphere (Konopliv et al., 2011a), but is well outside the ~230-km polar regions. However, this does not limit studies of the interior as the Vesta shape models are converted to spherical harmonic gravity fields assuming various interior layers of crust, mantle and core with differing densities. Evaluations of the interior models are then made on the ellipsoidal surface where the harmonics converge. Ellipsoidal harmonics (Garmier and Barriot, 2001) provide an alternate representation of the gravity field that can be mapped to the entire surface of Vesta (Park et al., 2013) as was done for the Asteroid Eros by the NEAR mission (Garmier et al., 2002).

The Dawn gravity science investigation uses the Doppler and range measurements to the spacecraft and optical landmark tracking from spacecraft images of Vesta to measure the gravity field and other parameters that affect the dynamics of the spacecraft orbit. The Doppler X-band is the primary data for gravity field and it measures subtle changes in the spacecraft velocity along the line-of-sight direction (Earth–Vesta) to an accuracy better than 0.1 mm/s. The primary benefit of the DSN range data is the improvement of the Vesta orbit about the Sun. The optical landmark tracking data also benefit the Vesta heliocentric orbit as well as the Dawn spacecraft orbit around Vesta and the orientation of Vesta. The Dawn spacecraft began collecting data at Vesta just before orbit capture on July 16, 2011. For this analysis, tracking data are processed from July 13, 2011 through July 25, 2012 at the conclusion of the second High Altitude Mapping Orbit (HAMO-2). The phases of the mission are divided into Approach to Vesta, Survey Orbit, HAMO, Low Altitude Mapping Orbit (LAMO) and HAMO-2 (see Table 1). The HAMO-2 phase was able to complete imaging of the northern portion of Vesta that was missing from previous phases, and thus enabled a complete global shape model. In this paper we use the shape model of Gaskell (private communication, 2012) that includes coverage during HAMO-2. The HAMO-2 phase does not significantly improve the gravity field but does contribute to the determination of the Vesta spin-pole nutation and precession.

The gravity field and mass of Vesta, the orbit of Vesta around the Sun, the orientation and spin of Vesta, the location of the optical landmarks on the surface of Vesta, and orbits of Dawn with spacecraft force model parameters are jointly determined in a global estimation procedure similar to previous gravity investigations (e.g., Konopliv et al., 2002 for NEAR at Eros, Konopliv et al., 2011b for Mars). The NEAR investigation of Eros was very similar to the Dawn investigation of Vesta in that it also relied heavily on optical landmark tracking to help determine the spacecraft orbit, spin pole and inertial tie to the shape model. The resulting gravity field for Eros was valid to harmonic degree 10. Likewise, the primary objective of the Dawn gravity investigation is to determine the gravity field of Vesta to 90-km half wavelength resolution or harmonic degree 10 (Konopliv et al., 2011a). The actual resolution of the gravity field is determined by the altitude of the LAMO mission phase. As a result, the final resolution of the gravity field is much better than the requirement and is near harmonic degree 20 or 42-km, which is slightly better than the simulated results (Konopliv et al., 2011a).

Prior to Dawn at Vesta, the possible values for the mass of Vesta were determined from close flybys of asteroids with Vesta (Michalak, 2000; Baer et al., 2008; see home.earthlink.net/~jimbaer1/astmass.txt; Kuzmanoski et al., 2010), as well as the effect of Vesta on the Mars orbit (Standish, 2001; Pitjeva, 2005; Konopliv et al., 2006, 2011b; Fienga et al., 2009 ; Kuchynka and Folkner, 2013), and the effect of Vesta on the orbit of Eros using the NEAR range data (Konopliv et al., 2002, 2011b). The assumed probable range of values for the Vesta GM was given by 17.3–17.8 km^3/s^2 from the latest studies. With the initial results from portions of the LAMO mission phase, the Dawn mass estimate is accurate to near 1 part in 10^6 from the gravity investigation (Russell et al., 2012).

2. Radiometric and optical measurements

The Vesta gravity field is measured by detecting its effect on the motion of the Dawn spacecraft, so essentially the spacecraft is the instrument for this investigation. The motion is measured using the telecommunications link between the spacecraft and the Deep Space Network (DSN) and the images from the onboard framing camera. The DSN station transmits the right-hand circularly polarized X-band link frequency at 7.179 GHz for uplink while the downlink signal, for science and engineering telemetry packets, is centered at 8.435 GHz. The two-way (same transmit and receive stations) and three-way (different receive station) coherent mode for radiometric Doppler tracking measures the spacecraft's velocity in the direction of Earth to typically ~0.05 mm/s or better at 10-s integration times by measuring the Doppler frequency shift in the received signal (for example, see Fig. 2 of Konopliv et al., 2011a). Fig. 1 displays the Dawn Doppler tracking residuals during the entire Survey and HAMO mission phases. Since we process the Dawn Doppler observables using a 60-s sample time, the RMS of the residuals are $\sim\sqrt{6}$ lower. This measure of the gravity science data quality depends on several factors such as the effects of media, the angular proximity of the radio beam to the Sun and the received signal-to-noise ratio (SNR) (Asmar et al., 2005). All Doppler and range data are calibrated at each DSN complex for daily Earth

Table 1
Phases of the mission to the conclusion of the lowest altitude LAMO phase and tracking and optical data processed for each phase. The number of observations given for the optical data represents the number of landmark observation pairs (sample, line). The typical number of landmarks in each image is given by the total observations divided by the number of images for that phase.

	Approach	Survey	HAMO	LAMO + PreLAMO coast	HAMO-2
Begin time	July 13, 2011 05:42	August 2, 2011 07:49	September 28, 2011 10:46	November 18, 2011 02:00	June 6, 2012 06:00
End time	July 28, 2011 12:46	August 31, 2011 21:39	November 2, 2011 11:04	May 01, 2012 12:00	July 25, 2012 15:00
Duration (days)	15.3	29.6	35.0	165.9	49.4
Number of data arcs	2	1	1	18	2
Number of Doppler data	8203	35,048	31,870	132,724	57,097
Number of range data	2694	9740	7017	10,311	11,382
Number of images/obs.	203	1102	2555	3511	2729
	2359	31,611	61,243	11,952	56,508
Altitude (km, 265-km sphere)	25,000–5214	2725–2737	663–701	169–324	650–714
Orbit period	7.37 days	2.87 days	12.17 h	4.25 h	12.18 h

Please cite this article in press as: Konopliv, A.S., et al. The Vesta gravity field, spin pole and rotation period, landmark positions, and ephemeris from the Dawn tracking and optical data. Icarus (2013), http://dx.doi.org/10.1016/j.icarus.2013.09.005

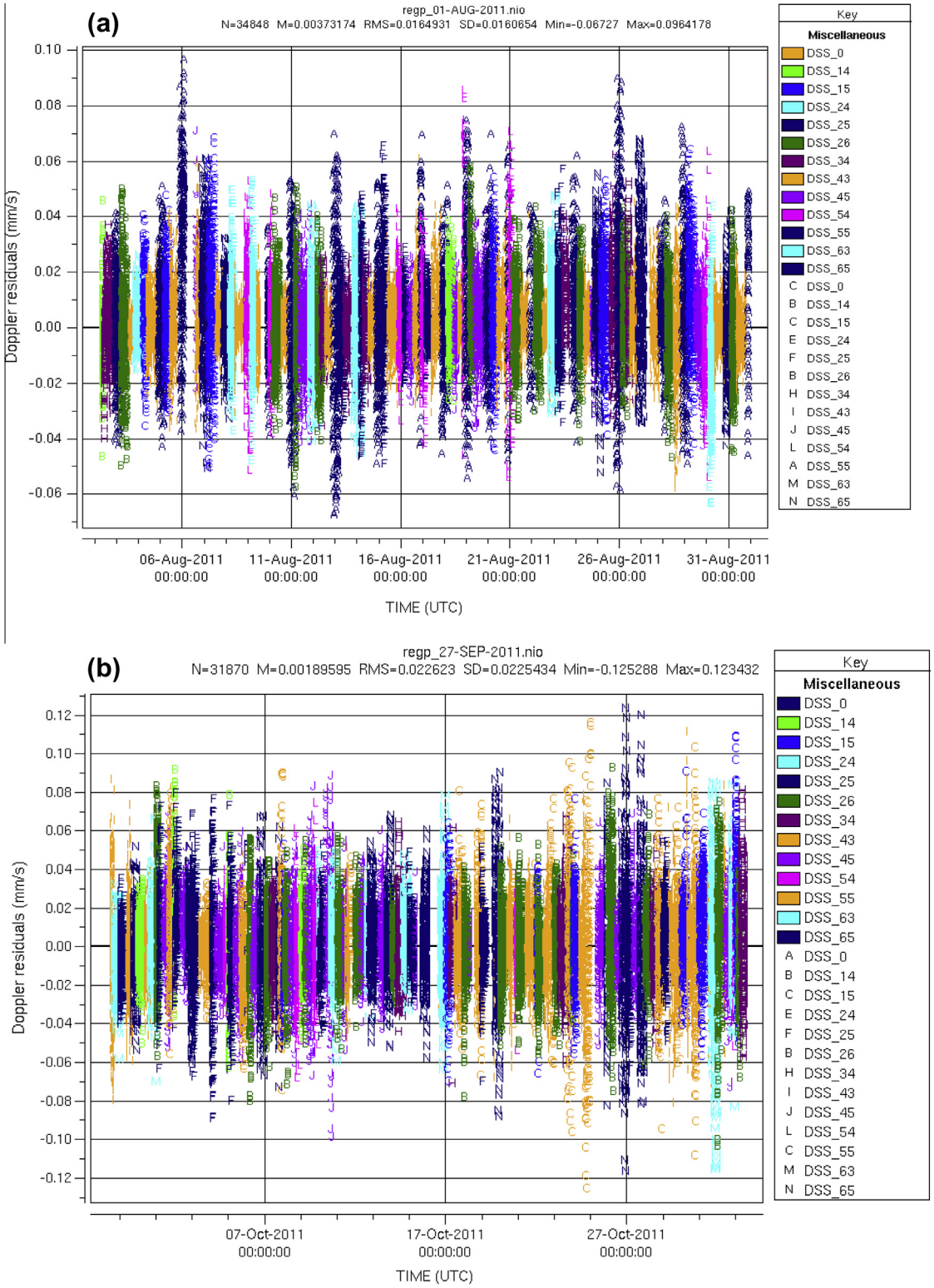

Fig. 1. Doppler 60-s residuals for the (a) Survey phase of the mission (29.6 days total) with an RMS noise of 0.016 mm/s and (b) HAMO phase of the mission (35.0 days) with RMS noise of 0.023 mm/s.

dry and wet troposphere corrections and daily Earth ionosphere calibrations based upon GPS measurements.

The main consideration for the accuracy of the Doppler is how close the signal passes by the Sun or the Sun–Earth–Vesta angle. The accuracy of the X-band signal starts to degrade significantly for Sun angles less than 20° (Konopliv et al., 2011a), and this occurs during the middle of the LAMO mission phase (see Fig. 2). Another consideration for the strength of the Doppler data is the geometry of the spacecraft orbit plane as viewed from the Earth and Sun, where typically the gravity field is better determined when viewed edge-on from the Earth as opposed to near face-on geometries. The viewing from both the Sun and Earth show favorable geometry for

Please cite this article in press as: Konopliv, A.S., et al. The Vesta gravity field, spin pole and rotation period, landmark positions, and ephemeris from the Dawn tracking and optical data. Icarus (2013), http://dx.doi.org/10.1016/j.icarus.2013.09.005

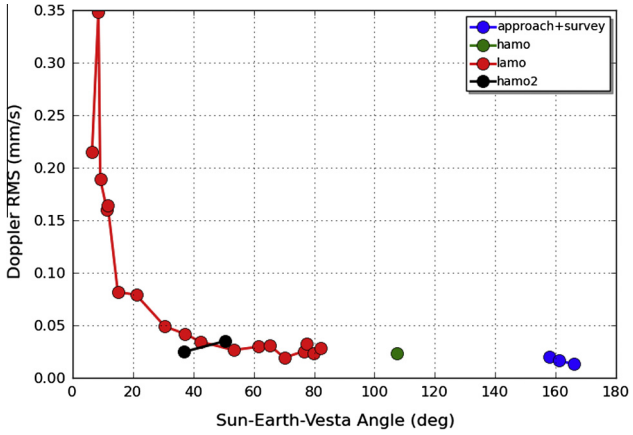

Fig. 2. Dawn 60-s Doppler residual noise as a function of Sun angle for each Dawn data arc.

Dawn (Fig. 3). The Dawn spacecraft uses a 1.52-m diameter paraboloid high gain antenna (HGA) that is fixed to the spacecraft (does not articulate) to downlink the science and engineering telemetry and has ample SNR margin to achieve the higher Doppler accuracy. However, for much of the mission duration the HGA is used for only several 8-h tracking passes per week since the spacecraft is nadir pointed to Vesta to collect science data. After further investigation, it was determined that the three (+X, +Z, −Z) low gain antennas (LGA) had just enough link margin with the 34-m DSN stations to collect sufficiently accurate Doppler data, and with the 70-m DSN antennas, the SNR error contribution was negligible. As a result there is nearly continuous Doppler tracking during all mission phases as seen in Fig. 1 where the vast majority of the tracking is acquired using the LGAs.

The optical landmark tracking data comes from the framing camera, which collected images of Vesta during all mission phases. The optical observation is the line and pixel location of a landmark in the image. The landmark is the vector from the center of Vesta to the center of a maplet (typically 99 × 99 pixels) that defines the landmark control-point. Each grid point or pixel of the maplet then has a local elevation relative to the control point determined in a separate stereophotoclinometry process (e.g., Gaskell et al., 2008). There are 155,000 landmark locations that define the shape of Vesta. Since it is not feasible to estimate all the landmarks in the global gravity solution, we selected 4000 landmarks uniformly distributed over the surface of Vesta (including the northern polar region >60°N which was imaged during the HAMO-2 phase). For these landmarks, the solution is for about 12,500 parameters (three body-fixed position locations for each landmark plus other parameters including, for example, spacecraft state and Vesta rotation and gravity). The landmark location can be determined in the camera image with an accuracy of about 0.25 pixel after correcting for pointing. This essentially ties the spacecraft's downtrack and crosstrack position to the Vesta surface with a typical accuracy of 150 m, 110 m, 60 m and 5 m for the Approach, Survey, HAMO and LAMO mission phases. Fig. 4 displays the optical residuals for the sample and line directions for HAMO and shows the typical RMS of 0.1 pixels. For HAMO and HAMO-2, camera images were processed every 5–10 min with an average of 20–25 landmarks processed for each image. The time between images was reduced to about 2 min during LAMO but with fewer landmark observations per image.

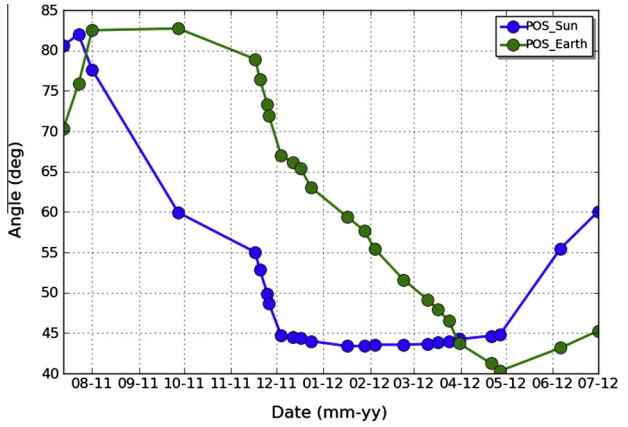

Fig. 3. Dawn orbit inclination in the plane-of-sky as viewed from the Earth and Sun for each Dawn data arc. Near edge-on orbits are given by inclinations near 90° and face-on orbits near 0°.

The time span and the amount of DSN tracking and optical data used for this analysis for the five different mission phases is given in Table 1. The Approach phase (first 15 days of data) provided the first sensitivity for the gravity that resulted in a 0.1% determination of the mass of Vesta and a 10–20% determination of the degree 2 gravity coefficients. During the Approach, there are several SEP thrust events from July 13 to July 23, 2011 that are modeled and adjusted in the estimation process, but after July 23, 2011 all processing of Dawn spacecraft data were taken during periods of time without any SEP thrusting. However, smaller maneuvers to de-spin the angular momentum wheels (AMDs) occurred on average every 2.3 days during Survey, 3.2 days during HAMO, typically once per day during LAMO, and every 2.1 days for HAMO-2.

3. Solution technique

The Vesta gravity field and related parameters are estimated jointly combining all the tracking and optical data for all phases of the mission. The observations are processed and solution generated using the JPL MIRAGE software set (a gravity processing version of the JPL Orbit Determination Program or ODP, Moyer, 1971, 2000) and the optical navigation software (e.g., Owen et al., 2001). It is the historical software set that was used for navigation at JPL (until the recent change to MONTE software program within the last few years), and has been used for all JPL gravity studies.

The equations of motion and variational partials (e.g. Tapley et al., 2004) for the estimated parameters are numerically integrated (variable order Adams method, Krogh, 1973) in MIRAGE for the nominal motion of the spacecraft in the inertial International Celestial Reference Frame (ICRF), which is nearly equivalent to the Earth's mean equator at the epoch of J2000 (within <100 mas, Folkner et al., 1994). MIRAGE then estimates the spacecraft position and velocity, gravity harmonic coefficients, and other parameters using a square root information weighted least-squares filter (or SRIF, see Bierman, 1977; Lawson and Hanson, 1995). The DSN and optical data are divided into separate time spans or data arcs for processing. The parameters that are estimated consist of arc-dependent variables (spacecraft position, AMDs, etc.) that are separately determined for each of the 24 data arcs (see Table 1) and global variables (e.g., gravity coefficients and landmark positions, with a total of more than 12,000 parameters) that are common to all data arcs. MIRAGE software is a parallelized code that merges only the global portion of the square root information matrix from all the arcs of the entire mission (24 arcs varying in length from 2 days to 35 days), but is equivalent to solving for the global parameters plus arc-dependent parameters of all the arcs. Kaula (1966) outlines the technique for partitioned normal matrices.

Please cite this article in press as: Konopliv, A.S., et al. The Vesta gravity field, spin pole and rotation period, landmark positions, and ephemeris from the Dawn tracking and optical data. Icarus (2013), http://dx.doi.org/10.1016/j.icarus.2013.09.005

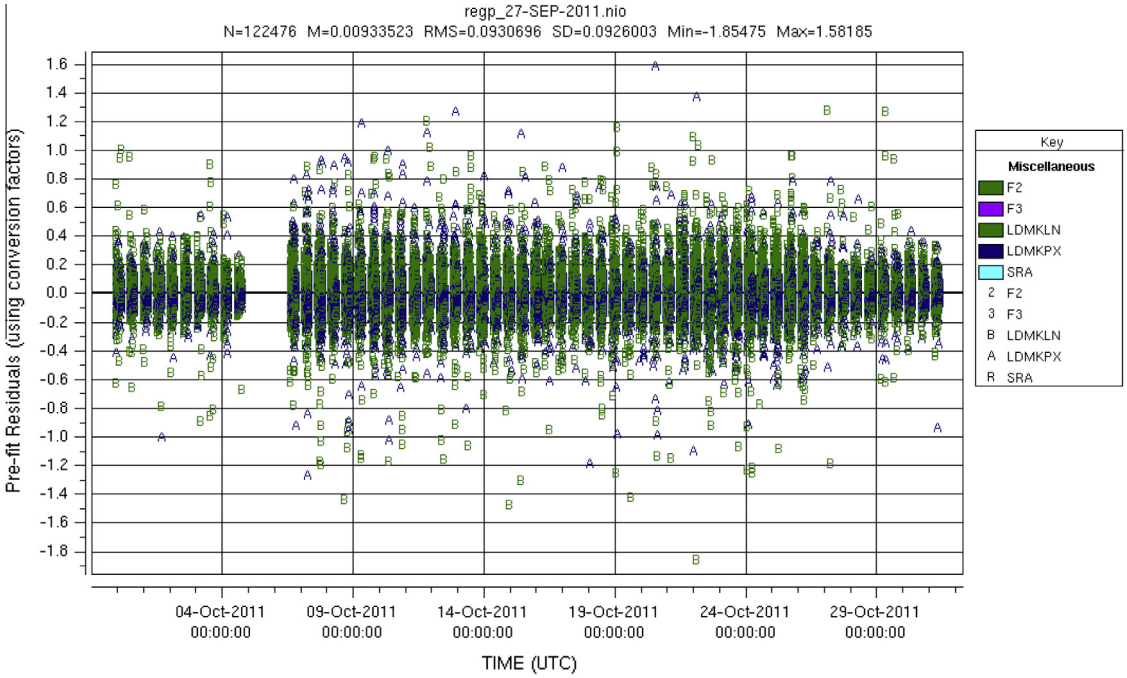

Fig. 4. Landmark optical residuals in pixels for the HAMO mission phase. The RMS of the residuals in both the sample (LDMKPX, blue) and line (LDMKLN, green) directions of the landmark image is a typical 0.1 pixels. (For interpretation of the references to color in this figure legend, the reader is referred to the web version of this article.)

For all but the HAMO-2 mission phase, the length of each data arc is chosen to be as long as possible. During both the Survey and HAMO mission phases, there are no spacecraft maneuvers other than small (~1 mm/s) AMD events, and so the entire phase can be processed as one data arc. For the LAMO phase, however, there is typically a spacecraft orbit trim maneuver once a week to adjust the spacecraft altitude. As a result, the data arc is broken at these times to avoid fitting through the SEP burns and possibly corrupting the gravity solution with burn errors. Although there are no burns during the HAMO-2 phase, the data are broken into two 25-day arcs instead of one 50-day arc to be consistent with the arc lengths of the Survey and HAMO phases.

The local parameters that are estimated for every arc are spacecraft position and velocity, solar pressure scale factors in three directions (in the Sun–spacecraft direction and the two orthonormal directions), scale factors on the a priori burn magnitudes of the AMDs, small velocity increments in all three spacecraft axes directions at the center of the time duration of the AMDs, stochastic white noise acceleration, small biases on any three-way Doppler passes (<0.1 mm/s), ranges biases per DSN range pass (1–2 m), and stochastic white noise pointing for the optical data. The solar pressure scale factors are allowed to adjust within 5% of the a priori value. The solar pressure model is a box-wing flat plate model that represents the spacecraft (Thomas et al., 2011) with three plates for the bus and two plates for the solar array. Pointing of the bus and solar arrays are given by spacecraft telemetry converted to NAIF C-Kernels (Krening et al., 2012). The solar arrays are Sun-pointed within 2° for the vast majority of the time given by all the arcs processed. The typical duration of the maneuver to despin the momentum wheels is about 15 min. Over the duration, the pulses are modeled as delta-velocity adjustments on the spacecraft orbit every 10–30 s depending on the mission phase. After a scaling adjustment on the pulse magnitudes from the spacecraft thrust model (~10%), a total delta-velocity correction of ~1 mm/s is applied at the AMD duration center. Small accelerations are also estimated to remove any remaining unmodeled non-gravitational forces such as spacecraft outgassing, spacecraft discharge of heat, and solar pressure model imperfections. The white noise stochastic acceleration time interval is 4.25 h for Survey, HAMO and HAMO-2 and 2 h for LAMO, with a prior magnitudes 5×10^{-13} km/s^2 or less (~1–2% of the solar pressure force). The pointing of the camera is adjusted for every image (there are typically many landmark observations in each image) in both image directions (sample and line) and a rotation or twist. The a priori uncertainty in the pointing is 0.005°, 0.005°, 0.002° (~1 pixel) for both sample, line and twist, respectively.

The global parameters estimated are a 20th degree and order spherical harmonic gravitational potential model and corresponding GM, the x, y, z position locations of the landmarks, three small rotation corrections of the camera frame with respect to the spacecraft frame (equivalent to ~1 pixel), the spin pole right ascension and declination and their rates and rotation rate, the specular and diffuse coefficients of the solar pressure model plates, and the LGA antenna locations.

The gravitational potential of Vesta is modeled by a spherical harmonic expansion in the body-fixed reference frame with normalized coefficients ($\overline{C}_{nm}, \overline{S}_{nm}$) that are given by (e.g., Heiskanen and Moritz, 1967; Kaula, 1966)

$$U = \frac{GM}{r} + \frac{GM}{r}\sum_{n=1}^{\infty}\sum_{m=0}^{n}\left(\frac{R_e}{r}\right)^n \overline{P}_{nm}(\sin\phi_{lat})\left[\overline{C}_{nm}\cos(m\lambda) + \overline{S}_{nm}\sin(m\lambda)\right]$$

where GM is the gravitational constant times the mass of the central body, n is the degree, m is the order, $\overline{P}_{nm}$ are the fully normalized associated Legendre polynomials, R_e is the reference radius of the body (265-km for Vesta), ϕ_{lat} is the latitude, and λ is the longitude. The gravity coefficients are normalized such that the integral of the harmonic squared equals the area of a unit sphere, and are related to the unnormalized coefficients as (Kaula, 1966; Lambeck, 1988)

$$\begin{pmatrix} C_{nm} \\ S_{nm} \end{pmatrix} = \left[\frac{(n-m)!(2n+1)(2-\delta_{0m})}{(n+m)!}\right]^{1/2} \begin{pmatrix} \overline{C}_{nm} \\ \overline{S}_{nm} \end{pmatrix}$$

Please cite this article in press as: Konopliv, A.S., et al. The Vesta gravity field, spin pole and rotation period, landmark positions, and ephemeris from the Dawn tracking and optical data. Icarus (2013), http://dx.doi.org/10.1016/j.icarus.2013.09.005

The degree one coefficients are zero, since the origin of the coordinate system is chosen to be the center of mass. The zonal coefficients are given by $\bar{J}_n = -\bar{C}_{n0}$.

4. Vesta gravity results

The Dawn spacecraft altitude determines the Vesta gravity resolution that can be observed. One can clearly see the improvement in resolution over the mission with the Survey, HAMO and LAMO phases. The RMS gravity spectrum is expected to follow a power law (Kaula, 1963) and is given by

$$M_n = \sqrt{\frac{\sum_{m=0}^{n}(C_{nm}^2 + S_{nm}^2)}{2n+1}} \approx \frac{K_{\mathrm{Vesta}}}{n^2}$$

where the constant $K_{\mathrm{Vesta}} = 0.011$ is scaled from the Earth value to Vesta using

$$K_{\mathrm{Vesta}} = K_{\mathrm{Earth}} \left(\frac{M_{\mathrm{Earth}}}{M_{\mathrm{Vesta}}}\right)^2 \left(\frac{R_{\mathrm{Vesta}}}{R_{\mathrm{Earth}}}\right)^4$$

Fig. 5 shows the gravity spectrum for the addition of each mission phase. The gravity resolution is determined by the harmonic degree at which the uncertainty in the spectrum equals the magnitude. For Survey, the Vesta gravity field is determined to harmonic degree 4, and improves to degree 8 for HAMO. The best resolution is degree 20 or 42-km half-wavelength resolution when LAMO data are included. The gravity solution with all data from all mission phases is given the name VESTA20H, and the GM, degree 2 and 3 values are listed in Table 2. The C_{21}, S_{21} coefficients are zero within their uncertainties, indicating there is no detectable offset between the principal axes and spin pole. The gravity spectrum agrees fairly well with the expected power law except for the first few degrees, which are dominated by the ellipsoidal shape of Vesta. From the latest shape volume and GM estimate, the bulk density is 3459 kg/m^3, consistent with Russell et al. (2012). The current error in the density is dominated by the volume uncertainty in the shape model (<0.1%), which has been reduced from previous results due to observation of the northern polar region during HAMO-2.

The gravity field as seen in Fig. 6 closely follows the gravity expected from nearly homogeneous topography, and it is not necessarily useful for interior modeling up to degree 20. As is the case for Eros (Konopliv et al., 2002) the differences between the gravity field and the gravity field determined from a three-layered shape

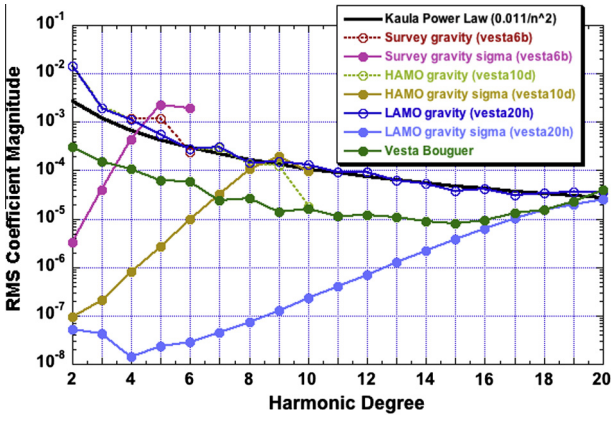

Fig. 5. Vesta gravity spectrum for each phase of the mission. The improvement in the gravity field resolution is evident for each progressively lower altitude from Survey, HAMO and LAMO. The differences between gravity and that modeled from the nominal three-layer shape ("Vesta Bouguer") is ~10× smaller than the gravity itself indicating minimal lateral density variations in Vesta. The three-layer model consists of homogeneous crust, mantle and core, with an ellipsoid of revolution defining the mantle and core shape.

Table 2
Spherical harmonic gravity coefficient values for the VESTA20H gravity solution up to degree 3 terms (normalized). The reference radius for the coefficients below is 265-km, and the prime meridian is defined by the Claudia crater. The uncertainty given is 3× the formal uncertainty to give more realistic errors.

Coefficient or parameter	Normalized value	Normalized uncertainty
GM (km^3/s^2)	17.288245	0.000012
J_2	3.1779397e−2	1.9e−8
C_{21}	1.23e−9	4.3e−9
S_{21}	−1.13e−9	4.3e−9
C_{22}	1.0139517e−3	3.5e−7
S_{22}	4.2469730e−3	8.2e−8
J_3	−3.3105530e−3	1.9e−8
C_{31}	2.0456938e−3	7.0e−8
S_{31}	1.6820966e−3	8.4e−8
C_{32}	6.5144047e−4	1.0e−7
S_{32}	−1.2177599e−3	5.5e−8
C_{33}	2.3849359e−3	2.1e−8
S_{33}	1.5466248e−4	2.9e−7

(or Bouguer coefficients) are much smaller than the actual gravity. The nominal shape model used is a three-layer crust, mantle and core model where each layer is homogeneous with the corresponding densities 3.0 g/cm^3, 3.17 g/cm^3, and 7.4 g/cm^3. The crustal density is chosen to minimize the Bouguer anomalies when considering all harmonic degrees, and the mantle and core densities are consistent with Russell et al. (2012). The mantle and core are both ellipsoids of revolution where the mantle is 257 × 207-km and the core has a flattening of 0.1 and a mean radius near 110-km. With these mantle and core shapes, the chosen mantle and core densities only affect the low degree even zonal contributions to the Bouguer anomalies and are an overall minimal effect. The Bouguer anomalies, shown spatially in Fig. 7 and spectrally in Fig. 5, also show this difference is an order of magnitude smaller than the gravity signal. The uncertainty in the Bouguer coefficients equals the magnitude at about degree 15, and suggests interior models can be evaluated to this resolution (55-km half-wavelength). The agreement of gravity with gravity from homogeneous shape is also shown by the strong correlations (see Fig. 8) between the corresponding coefficients.

The interpretation of the Bouguer anomalies for various regions is limited in part by the uncertainties in the gravity field. Fig. 9 shows the uncertainties of the gravity field mapped to the same 290 × 265-km ellipsoid of the gravity map where errors are given through degree 15 as suggested by Fig. 5. The maximum errors are at the polar regions with higher errors near 10-mgal at the south pole due to higher spacecraft altitude (see Fig. 10). This is significantly smaller than the Bouguer anomalies near Rheasilvia of ~200 mgals. If the gravity is mapped to a 290-km sphere, the gravity uncertainties over the sphere are fairly uniform at 1–2 mgals and match the equatorial errors of Fig. 9. The gravity errors increase significantly when all degree 20 coefficients are included. The corresponding error in the polar regions for the 290 × 265 ellipse is 170 mgals, and is a significant portion of the Bouguer anomaly. With the use of ellipsoidal harmonics, the gravity field and errors can be mapped much closer to the surface of Vesta in the polar regions (Park et al., 2013).

The accuracy of the Dawn orbits varies according to mission phase. Since the data arcs are chosen to be as long as possible, all but one arc boundary is caused by a spacecraft maneuver. Overlap error analysis to measure orbit accuracy is corrupted by the maneuvers. However the local covariance orbit estimate gives a general idea of the orbit accuracy. The orbit error is on the order of 10-m for the Survey phase, 1 m for the HAMO and HAMO-2 phases, and one to several hundred meters for LAMO depending on the arc length and whether optical data are available.

Please cite this article in press as: Konopliv, A.S., et al. The Vesta gravity field, spin pole and rotation period, landmark positions, and ephemeris from the Dawn tracking and optical data. Icarus (2013), http://dx.doi.org/10.1016/j.icarus.2013.09.005

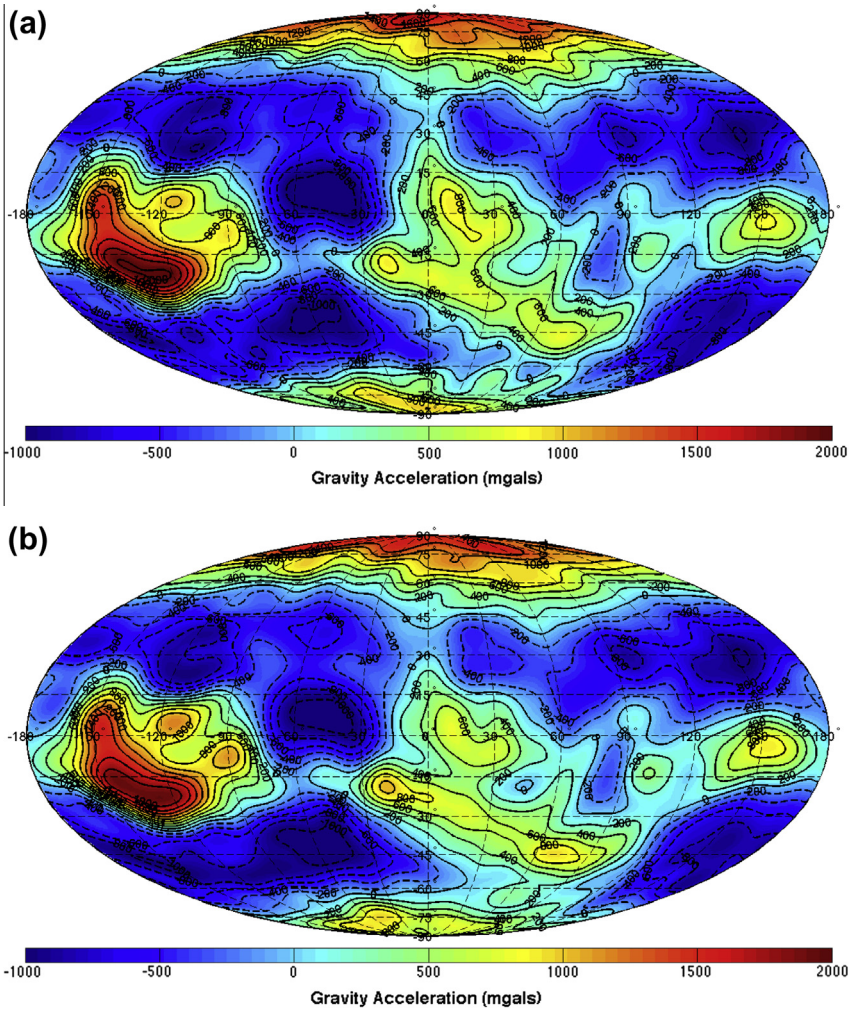

Fig. 6. The Vesta (a) radial gravity solution and (b) radial gravity from the nominal three-layer shape model mapped to a 290 × 265-km ellipsoid surface through degree 20. The J_2 coefficient has been removed. The maximum and minimum range is given by 2100 mgals at the large equatorial high near 126°W longitude and −1270 mgals also near the equator at 44°W.

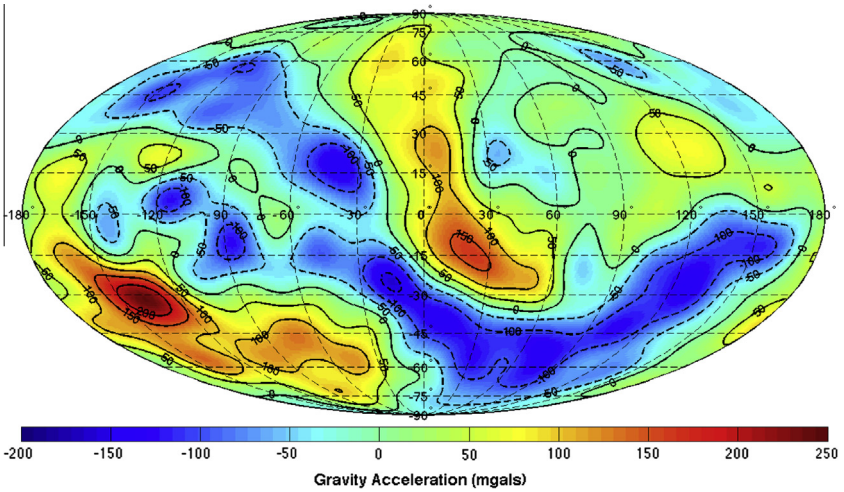

Fig. 7. The Vesta Bouguer anomaly mapped to the same 290 × 265-km ellipsoid through harmonic degree 15. The anomaly shown is the observed gravity minus the gravity computed from the nominal three-layer homogeneous crust, mantle and core shape model.

Please cite this article in press as: Konopliv, A.S., et al. The Vesta gravity field, spin pole and rotation period, landmark positions, and ephemeris from the Dawn tracking and optical data. Icarus (2013), http://dx.doi.org/10.1016/j.icarus.2013.09.005

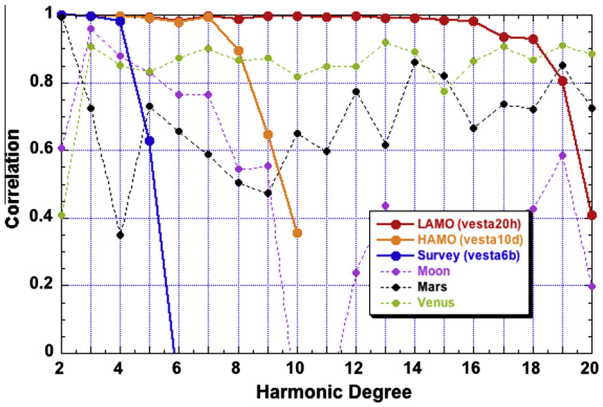

Fig. 8. Correlation between gravity and gravity from shape. The shape model is the nominal three-layer core, mantle crust model. The correlation between gravity and topography for Venus, Moon, and Mars are also given to demonstrate the strong match between shape and gravity for Vesta.

5. Vesta spin pole and rotation period

The dynamics of the spacecraft orbit are strongly affected by the Vesta spin pole location and rotation rate through the orientation of the gravity field, so any mis-orientation of Vesta is clearly seen in the DSN Doppler data, thus requiring an estimation of the Vesta orientation. The spin pole is given in the ICRF with the IAU coordinate frame definition of right ascension α and declination δ (see Fig. 2 of Archinal et al., 2011). Prior to the Dawn mission the best pole determination was from Hubble images (Thomas et al., 1997; Li et al., 2010) and the rotation period was obtained from many years of light-curve data (Drummond et al., 1988). The initial results from Dawn greatly reduced the uncertainty in the pole and indicate a significant shift in the rotational period (Russell et al., 2012).

The full expressions for the modeled right ascension and declination of the Vesta spin pole including the terms for precession (secular) and nutation (periodic terms as given by Rambaux (2013)) are given by

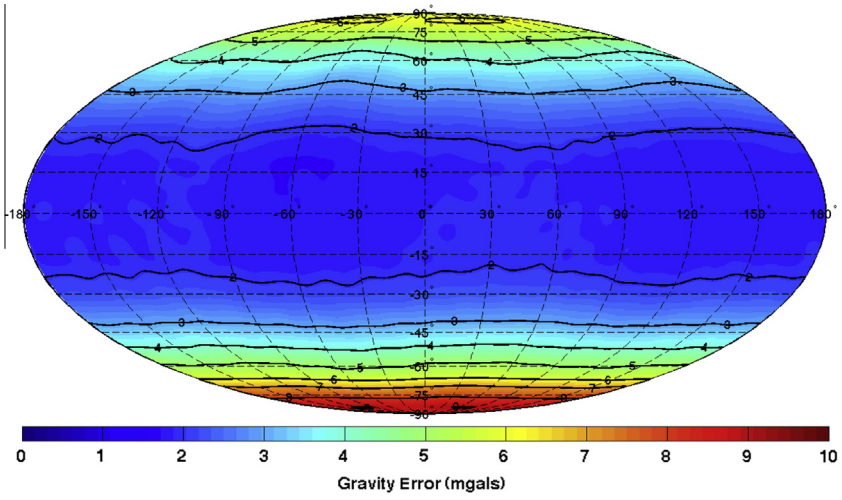

Fig. 9. The Vesta gravity field surface radial gravity error through degree 15 mapped to the 290 × 265-km ellipsoid.

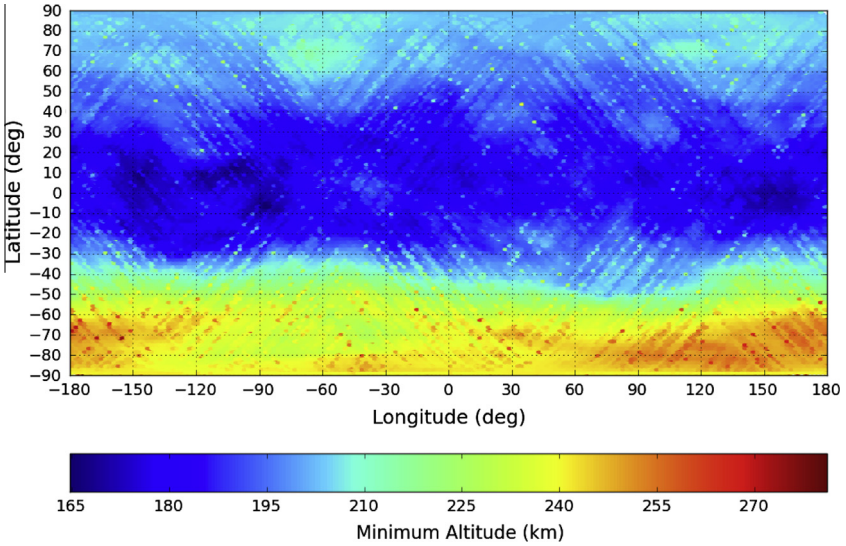

Fig. 10. Spacecraft minimum altitude of all spacecraft groundtracks relative to the actual Vesta surface for the LAMO mission phase.

Please cite this article in press as: Konopliv, A.S., et al. The Vesta gravity field, spin pole and rotation period, landmark positions, and ephemeris from the Dawn tracking and optical data. Icarus (2013), http://dx.doi.org/10.1016/j.icarus.2013.09.005

$$\alpha = \alpha_o + \dot{\alpha}_o T + \sum_{n=1}^{4} \alpha_{sn} \sin(\omega_n d + \phi_{sn})$$

$$\delta = \delta_o + \dot{\delta}_o T - \sum_{n=1}^{4} \delta_{cn} \cos(\omega_n d + \phi_{cn})$$

where T and d are centuries and days past J2000. The orientation parameters that are estimated as part of the global gravity solution are the spin pole location (α_o, δ_o), spin pole precession $(\dot{\alpha}_o, \dot{\delta}_o)$, and rotation rate. The Vesta nutation (Rambaux, 2013) is modeled but the amplitudes are not estimated. The associated constants for the nutation model $(\alpha_{sn}, \delta_{cn})$ are given in Table 3. Only the first four frequencies ω_n (up to four times per Vesta orbit) are included, and the remaining higher frequency terms are all less than 10 mas. Fig. 11 shows the right ascension and declination variations and their rates due to nutation for the time period where Dawn is at Vesta.

The Vesta precession rate $\dot{\psi}$ due to the gravitational torque from the Sun is given by the expression (e.g., Ward and Hamilton, 2004)

$$\dot{\psi} = \frac{3}{2}\left(\frac{n^2}{\omega_s}\right)\frac{C - (A+B)/2}{C}\cos\epsilon$$

where n is the mean motion of Vesta, ω_s is the spin rate, ϵ is the obliquity of Vesta equator, and $A < B < C$ are principal moments of inertia. This can be rewritten in terms of

$$C - (A+B)/2 = J_2 M R^2 \text{ and } C = \overline{C} M R^2$$

$$\dot{\psi} = \frac{3}{2}\left(\frac{n^2}{\omega_s}\right)\frac{J_2}{\overline{C}}\cos\epsilon$$

where $\overline{C}$ is the dimensionless polar moment of inertia. When the unnormalized oblateness J_2 is rescaled to the equatorial radius $R_{\text{mean}} = \sqrt{(a^2+b^2+c^2)}$, where a, b and c are the ellipsoidal radii (see Table 4), the normalized mean moment for a homogeneous ellipsoid is $\bar{I} = 0.4$ and the corresponding polar moment is $\overline{C} = 0.4517$. The best-fit ellipsoid mean radius of 264.0 km is close to the 265 km value we adopt. Using the values in Table 4 and a uniform density triaxial ellipsoid ($\bar{I} = 0.4$), the precession rate is $\dot{\psi} = 0.348786$ deg/cty. The modeled precession rate of the spin pole in the IAU coordinate frame is

$$\frac{d\alpha}{dt} = \dot{\psi}[\cos(\alpha_n - \alpha)\cos(\delta_n)\tan(\delta) - \sin(\delta_n)] = -0.594381\dot{\psi}$$

$$\frac{d\delta}{dt} = \dot{\psi}[\sin(\alpha_n - \alpha)\cos(\delta_n)] = -0.137681\dot{\psi}$$

where α_n and δ_n are the right ascension and declination of the Vesta orbit pole with the nominal values of the spin and orbit pole for January 1, 2012 in Tables 4 and 5. The modeled precession for a uniform density ellipsoid is

$$\frac{d\alpha}{dt} = -0.207311 \text{ deg/cty}$$

$$\frac{d\delta}{dt} = -0.048021 \text{ deg/cty}$$

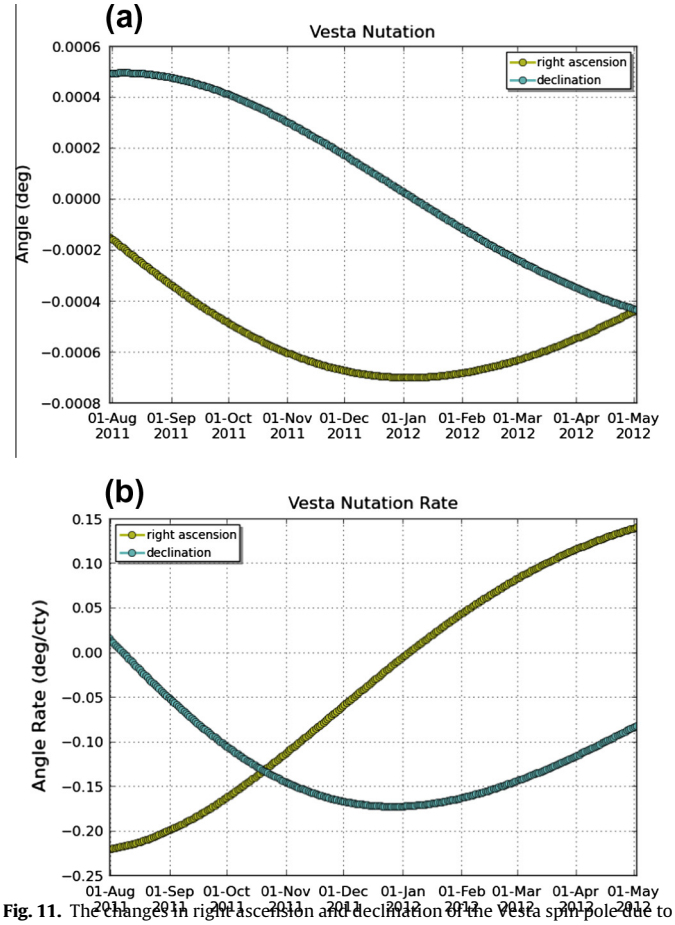

Fig. 11. The changes in right ascension and declination of the Vesta spin pole due to modeled nutation (Table 3) of the pole caused by the gravitational torque from the Sun. The nutation amplitudes are for the case where a homogeneous Vesta is assumed (i.e., dimensionless polar moment of inertia $\overline{C} = 0.4517$). Amplitudes are proportional to 1/C. The (a) angle and (b) angle rate changes are shown for the time Dawn is at Vesta.

Note that the declination rate for nutation (Fig. 11) is about four times as large as the declination rate for precession. The precession rate and nutation amplitudes are inversely proportional to polar moment and increase as mass is moved to the center of Vesta, as is the case for a core. In all cases the ratio of the precession right ascension rate to declination rate is constant. In our nominal solutions, we fix the solution for the rates $(\dot{\alpha}_o, \dot{\delta}_o)$ to have this ratio (4.31709). We also generate solutions where the direction of the precession is also estimated (i.e., not constrained by the ratio) to evaluate the robustness of the solution.

The nominal Vesta fixed pole and rotation rate solution is the first solution shown in Table 5 and includes DSN and optical data for all mission phases. All solutions in this table estimate only the spin pole location where the precession and nutation terms are not included in the rotation model. This nominal solution is recommended for processing that does not require the accuracy of the precession and nutation models, which is the case for the

Table 3
Vesta nutation parameters for right ascension (RA) and declination (DEC). The parameters listed are modeled but not estimated. The amplitudes given are for the uniform density case with the dimensionless polar moment of inertia $\overline{C} = 0.4517$ and approximately scale with the inverse of $\overline{C}$.

Index	RA amplitude α_{sn} (mas)	DEC amplitude δ_{cn} (mas)	RA phase ϕ_{sn} (deg)	DEC phase ϕ_{cn} (deg)	Frequency (deg/day)
$n = 1$	937.71	424.37	168.51	−120.92	0.27154951
$n = 2$	1635.55	1814.32	26.83	20.81	0.54312774
$n = 3$	344.75	381.17	5.91	1.12	0.81465787
$n = 4$	56.23	62.10	−14.27	−18.71	1.08618845

Please cite this article in press as: Konopliv, A.S., et al. The Vesta gravity field, spin pole and rotation period, landmark positions, and ephemeris from the Dawn tracking and optical data. Icarus (2013), http://dx.doi.org/10.1016/j.icarus.2013.09.005

Table 4
Constants for the calculation of modeled Vesta precession and nutation.

Parameter	Nominal value	Note
J_2	0.071060892	Unnormalized VESTA20H oblateness at R = 265 km
C_{22}	0.002818457	Unnormalized VESTA20H $\sqrt{C_{22}^2 + S_{22}^2}$ at R = 265 km
R_{eq}, R_{mean}	280.9 km 264.0 km	Using best-fit ellipsoid a = 284.50 km, b = 277.25 km, c = 226.43. However, we adopt R_{mean} = 265 km
$\overline{C} - \overline{A}$	0.076698	Difference in normalized principal moments, $\overline{C} - \overline{A} = J_2 + 2C_{22}$
$\overline{C} - \overline{B}$	0.065424	Difference in normalized principal moments, $\overline{C} - \overline{B} = J_2 - 2C_{22}$
n	0.271587 deg/day	Vesta mean motion from latest Vesta ephemeris solution (see Table 6)
ϵ	27.46241136 deg	Vesta obliquity from latest pole solution (Table 5) and Vesta orbit solution (Table 7)
α_n	288.170429	Vesta orbit pole right ascension from latest ephemeris solution (Table 7)
δ_n	67.256883	Vesta orbit pole declination from latest ephemeris solution (Table 7)

Table 5
Vesta orientation solution when precession and nutation are not included in the rotation model. Given uncertainties represent realistic errors that are 3× the formal sigmas. The estimate of the polar moment is given for case where the pole rate is estimated.

	α (deg)	δ (deg)	dW/dt (deg/day)
Nominal solution without modeled precession and nutation	309.03300 ± 0.00003	42.22615 ± 0.00002	1617.3331235 ± 0.0000005
Pole and spin rate solutions prior to Dawn			
Thomas et al. (1997) and Drummond et al. (1988)	301 ± 5	41 ± 5	1617.332776 ± 0.00007
Li et al. (2010)	305.8 ± 3.1	41.4 ± 1.5	
Solutions without precession and nutation to show pole and spin rate solution stability			
DSN only (all mission phases)	309.03298 ± 0.00003	42.22618 ± 0.00002	1617.3331238 ± 0.0000006
DSN only (LAMO phase only)	309.03308 ± 0.00003	42.22622 ± 0.00002	1617.3331242 ± 0.0000006
DSN + optical (no LAMO)	309.03230 ± 0.00009	42.22615 ± 0.00007	1617.3331344 ± 0.0000030

Table 6
(a) The secular rates of the Vesta spin pole from modeled precession and nutation for two different dimensionless polar moments of inertia $\overline{C} = 0.4517$ (uniform ellipsoid) and $\overline{C} = 0.42$ (three-layer model with 110-km 7.4 g/cm^3 core). The nutation rates are for the February 1, 2012 in the middle of LAMO. The units of right ascension rates ($d\alpha/dt$) and declination rates ($d\delta/dt$) are deg/cty. (b) The estimated Vesta pole rates for various combinations of data and with and without nutation modeled. Given uncertainties represent 3× the formal sigmas.

$\overline{C}$	Model precession $d\alpha/dt$	Model precession $d\delta/dt$	Model nutation $d\alpha/dt$	Model nutation $d\delta/dt$	Total model $d\alpha/dt$	Total model $d\delta/dt$
(a)						
0.4517	−0.2073	−0.0480	0.0459	−0.1623	−0.1614	−0.2103
0.42	−0.2230	−0.0516	0.0494	−0.1745	−0.1736	−0.2261

	Estimated $d\alpha/dt$	Estimated $d\delta/dt$
(b)		
DSN + optical (all mission phases) No nutation model	−0.1358 ± 0.038	−0.1248 ± 0.021
DSN only (all mission phases) No nutation model	−0.1606 ± 0.049	−0.1136 ± 0.028
DSN + optical (LAMO only) No nutation model	−0.1218 ± 0.055	−0.1811 ± 0.044
DSN + optical (all mission phases) Nutation model ($\overline{C} = 0.4517$)	−0.1439 ± 0.038	−0.0471 ± 0.021
DSN only (all mission phases) Nutation model ($\overline{C} = 0.4517$)	−0.1373 ± 0.049	−0.0564 ± 0.028

generation of the Vesta shape models from images. The epoch of the spin pole location and rates are January 1.5, 2000 as in the IAU definition. Several solutions are generated to test the stability of the pole and rotation values. With the combination of DSN and optical data, the uncertainties in the right ascension and declination are comparable and are known to better than 0.0001° during the Dawn stay at Vesta. The rotation rate for Vesta is very stable across various combinations of data and shows an increase in spin rate of ~5× the previous light-curve uncertainties. The strongest information content for the spin pole and rotation rate is from the Doppler data during the LAMO phase, and the rotation rate solution with DSN LAMO only agrees very well with the solution from DSN plus optical data for the joint Survey, HAMO and HAMO-2 mission phases.

The predicted right ascension and declination rates for the precession and nutation models are given in Table 6a. Rates are shown for two polar moment values, $\overline{C} = 0.4527$ for a uniform ellipsoid and $\overline{C} = 0.42$ for the nominal three-layer model with a 110-km core. Both rates are inversely proportional to $\overline{C}$. The observed (or estimated) precession pole rates are shown in Table 6b for cases with and without the nutation included in the rotation model. From the solutions we see that precession and nutation are partly detected. The estimated pole rates are about 70–85% of the predicted rates from the precession and nutation models, and thus cannot constrain the polar moment or detect a Vesta core. An extended stay at Vesta (2–3 years) would have been required to sufficiently determine $\overline{C}$. For example, simulations indicate a LAMO mission phase with twice the time reduces the polar moment

Please cite this article in press as: Konopliv, A.S., et al. The Vesta gravity field, spin pole and rotation period, landmark positions, and ephemeris from the Dawn tracking and optical data. Icarus (2013), http://dx.doi.org/10.1016/j.icarus.2013.09.005

uncertainty by 3×. For the case where the nutation model is not included in the estimation of the rates, the LAMO data only solution allows a direct comparison to the predicted rates on February 1, 2012. When the nutation model is included in the rotation model (but not estimated) we see that the precession right ascension rate is ~70% of the predicted precession (−0.2073 deg/cty) for a homogeneous Vesta and the declination rate is consistent with either a homogeneous Vesta (−0.0480 deg/cty) or Vesta with a core (−0.0516 deg/cty).

The nominal gravity field VESTA20H fixes the precession and nutation model to the homogeneous Vesta case of $\overline{C} = 0.4527$ (see Table 6a for the precession rates while the nutation model is given by Table 3 and Fig. 11). The rotation parameters estimated are the pole epoch position ($\alpha = 309.0587°$, $\delta = 42.2319°$) and the rotation rate ($\omega = 1617.333128$ deg/day). The prime meridian ($W_0 = 74.57621°$) is then chosen to minimize differences between the landmark position solutions and those from the nominal shape model.

6. Shape corrections from landmark estimates

The images of landmark features on Vesta tie the spacecraft location to the surface in the two orthogonal directions of the camera frame. Since the camera is mostly nadir pointed the images provide information for the position of the spacecraft along the velocity direction and normal to the orbit plane. The accuracy of the landmark location and spacecraft orbit estimates are expected to be better than one pixel. The pixel size of the camera, which is 0.00534°, is 19-m for LAMO 220-km average altitudes. Once pointing corrections are applied, the residual fit of the landmark observations is typically better than 0.25 pixels (or 5-m for LAMO). For landmarks that are well observed in multiple images, this matches the typical uncertainty in the filter output for global combined estimate of landmarks, gravity, and spacecraft epoch state. Again, images are processed from all phases of the Dawn mission except for HAMO-2, which will be processed in future efforts.

The a priori landmark positions are given by the shape model, which is derived from the images using stereophotoclinometry or SPC (Gaskell et al., 2008). In the process of determining the shape model using SPC, the spacecraft pointing, orbit locations, and image maplets (with a central landmark vector) are adjusted. The initial spacecraft orbits are in a coordinate frame with the center-of-mass of Vesta as the origin. Either the Dawn navigation team or the gravity science investigation (this paper) provides the orbits. The result is a shape model that is in a frame close to the center-of-mass. The purpose of this process is to readjust the landmark locations when including additional DSN data and dynamically estimating the gravity field and Vesta orientation. The intent is to provide a more complete inertial tie of the shape model to the center-of-mass and assess any potential long-wavelength errors in the shape model. Since the landmarks are part of the global gravity solution, their consistency with the SPC model is an indirect check of the long wavelength gravity quality.

The location of the center-of-figure (COF) with respect to the center-of-mass for the post HAMO-2 uniform shape model is −0.333, −1.409, −0.003 km in the x, y, z body-fixed directions where the Claudia crater defines the prime meridian (Russell et al., 2012), and corresponds to the offset in center-of-mass for a homogeneous density. The shape model in this case is well defined up to latitude 60°N, with the Thomas et al. (1997) model filling in the northern polar gap. For the nominal three-layer model with crust density 3.0 g/cm^3, mantle 3.17 g/cm^3, and core 7.4 g/cm^3, the location of the COF reduces to −0.289, −1.222, −0.002 km. Either case indicates the level of non-uniformity of the Vesta mass distribution. For example, in order to match the observed COF offset, the center of the core and mantle in the three-layer model must be shifted by 2.2, 9.7, and −1.3 km from the origin in the center-of-mass frame. Of course, other mass variations in the mantle or crust could completely explain the offset.

Next we look to compare the estimated landmarks with the SPC shape in similar fashion to the NEAR investigation (Konopliv et al., 2002). The differences between the two techniques given by the estimated landmark locations from gravity and the nominal shape model from SPC show a shift downward for the SPC model in the z-coordinate as shown in Fig. 12a. The nearly constant 70-m offset represents the uncertainty in either or both methods, but once the constant offset is accounted for, then the shape model differences are about 10-m. The large scatter in landmark positions near the shadow boundary at 60°N shows the degraded landmark ties due to lighting conditions.

The differences in the x and y coordinates are also near 10-m once corrections are applied (see Fig. 12b). The epoch prime meridian W_o in the global solution for gravity is chosen to minimize the x and y differences between the SPC shape model and the landmark estimates. In this case, the gravity solution is then consistent with the shape model. After adjustment of the prime meridian, the RMS differences between the estimated landmarks and shape model is 12.5-m. Currently a direct scaling factor of 0.99997 times the landmark estimates is required to reduce RMS differences to 11.0-m, or alternatively the SPC derived shape model must be enlarged by 1.00003 to match the estimated landmarks. This scale factor may or may not be real and depends on the camera distortion parameters. If the corrections for camera distortion are removed the scale

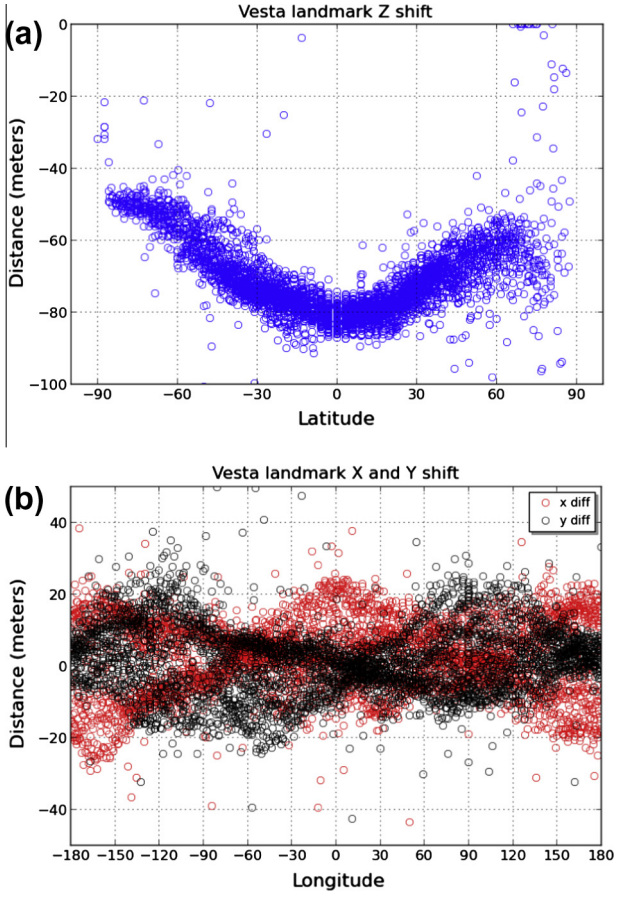

Fig. 12. Estimated landmark positions from the global gravity solution minus the a priori locations given by the SPC shape model (Gaskell, private communication, 2012) for the (a) z-coordinate and (b) the x and y coordinates.

Please cite this article in press as: Konopliv, A.S., et al. The Vesta gravity field, spin pole and rotation period, landmark positions, and ephemeris from the Dawn tracking and optical data. Icarus (2013), http://dx.doi.org/10.1016/j.icarus.2013.09.005

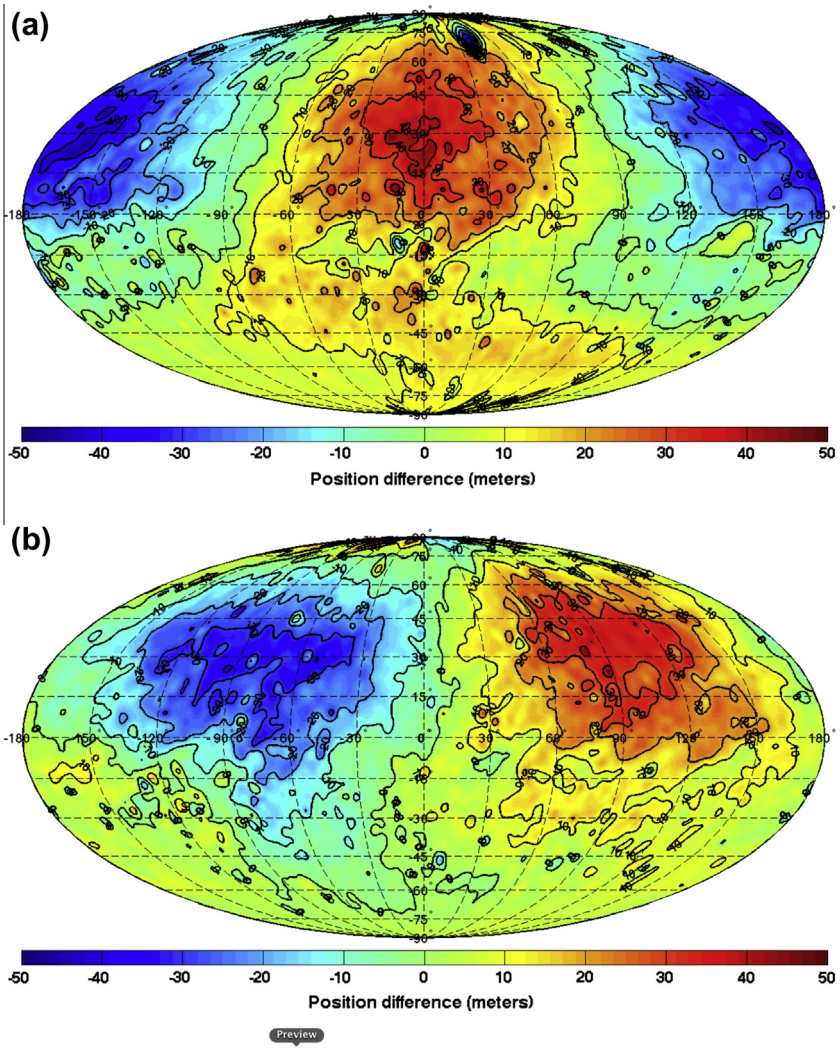

Fig. 13. Corrections for landmark locations as a function of latitude and longitude for the (a) x and (b) y components of the positions. Although small, long wavelength structure is visible in the corrections.

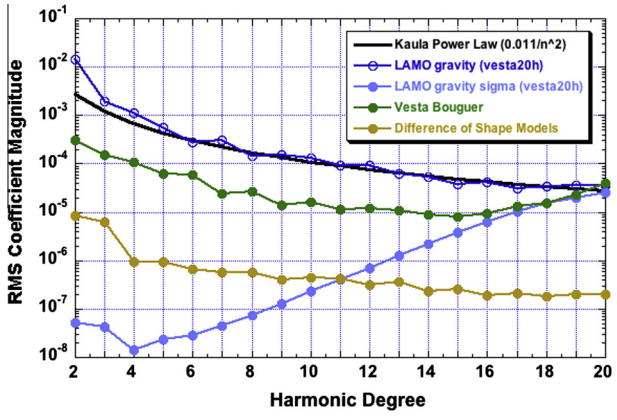

Fig. 14. The effect of adjusting the shape model on the gravity fields derived from three-layered crust, mantle and core shape model. The two gravity models differenced are the gravity from the original SPC shape model and the shape model adjusted to match the estimated landmark locations in the global gravity solution.

factor indicated a noticeably greater correction of 0.99992. So the differences in the shape model may be partly explained by camera distortion effects. With x and y position differences mapped to the surface (Fig. 13), the long wavelength correction, although small, becomes evident.

The differences in the estimated landmark locations with the SPC derived shape model can also be used to determine corrections to the gravity field derived from the SPC shape model. The estimated corrections are added to the SPC shape model, the shape is then converted to gravity using a three-layer model assumption, and then differenced with the original gravity derived from SPC shape using the same three-layer assumptions. The gravity from shape differences in Fig. 14 is well below the Bouguer anomalies as expected since the shape changes at the 0.1% level. The corresponding accumulated Bouguer anomaly error due to shape when mapped to the 290×265-km ellipsoid is 4 mgals, a negligible effect.

7. Vesta ephemeris improvement from dawn range data

The ephemeris or heliocentric orbit of Vesta is an important model that must be accounted for in the generation of the gravity solution. Mismodeling of the ephemeris results in significant aliasing in the gravity coefficients. The initial Vesta ephemeris accuracy from historical data is near 20-km near encounter in the Vesta–Earth direction and introduces systematic trends in the Doppler residuals of about 2 mm/s. The over 9 months of Dawn

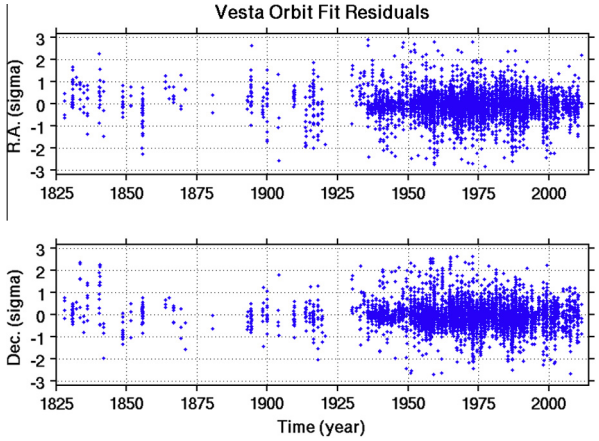

Fig. 15. Post-fit normalized residuals for optical data used in the new orbit solution for Vesta.

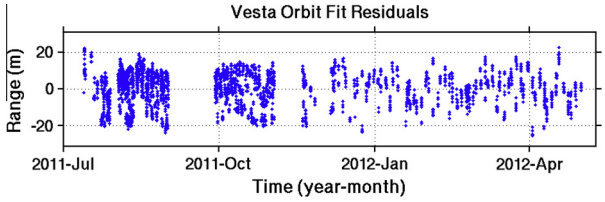

Fig. 16. Post-fit residuals for Dawn range data used in the new orbit solution for Vesta, shown in meters. The Dawn range data have been shifted to the Vesta center-of-mass and residual error is mostly due to Dawn spacecraft orbit error. Raw range data measurements to the Dawn spacecraft have an accuracy better than one meter.

range data are used to adjust the Vesta ephemeris using the same technique applied to the Mars ephemeris (Konopliv et al., 2011b). Similar methods also were used to improve the orbit of near-Earth Asteroid 433 Eros from NEAR spacecraft range data (Konopliv et al., 2002).

The range data to the Dawn spacecraft from multiple DSN stations are shifted from the spacecraft position to the center-of-mass of Vesta by resolving the round trip light equation (Moyer, 2000). The range observation is then equivalent to a radar bounce observation to the center of Vesta. The two main error sources in the observation are any errors in the spacecraft orbit and delay in the range measurement due to solar plasma. The latter is significant due to solar conjunction near the end of the LAMO mission phase.

Vesta's heliocentric orbit was computed using JPL's asteroid orbit determination code (Yeomans et al., 1992) with available optical astrometry (6851 measurements over the years 1827–2012) and converted Dawn spacecraft range data (2977 X-band measurements from 2011-July to 2012-May representing every 10th Dawn

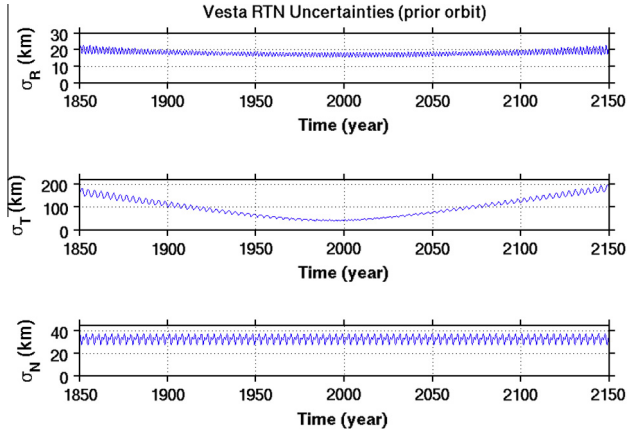

Fig. 17. Formal 1-sigma uncertainties in the heliocentric RTN coordinate system for Vesta's prior orbit solution.

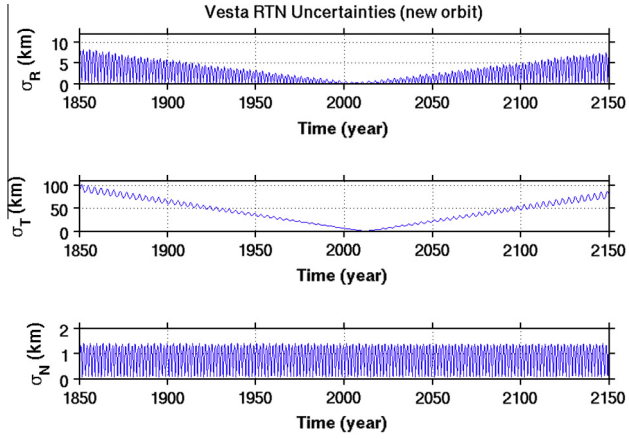

Fig. 18. Formal 1-sigma uncertainties in the heliocentric RTN coordinate system for Vesta's new orbit solution using Dawn range data.

range observation). Optical data were weighted appropriately based on a model described by Chesley et al. (2010), with weights ranging from about 3 to 0.2 arcsec. Recent optical data were further improved by taking into account known star catalog biases (Chesley et al., 2010). Dawn range data were weighted at 15 m, a level consistent with post-fit residuals and uncertainties in the Dawn spacecraft orbit relative to Vesta. Residuals in the optical and range data used in the orbit fit are shown in Figs. 15 and 16, respectively. The dynamical model used in the JPL asteroid orbit determination code considers perturbations from all the planets, the Moon, and Pluto from JPL's planetary ephemeris DE-423 (Folkner, 2010) and the 15 most massive asteroids (excluding Vesta): 1 Ceres, 2 Pallas, 10 Hygiea, 3 Juno, 6 Hebe, 7 Iris, 15

Table 7
Vesta's heliocentric ecliptic J2000 osculating orbital elements and associated formal uncertainties at epoch 2012-January-01.0.

Element	Prior solution value	New solution value	Prior solution uncertainty 1-sigma	New solution uncertainty 1-sigma	Uncertainty ratio
e	0.088267100483	0.088267108519	2.68×10^{-8}	1.46×10^{-10}	180
q (AU)	2.15310006576	2.15310004785	6.32×10^{-8}	1.15×10^{-9}	55
T (JD)	2455593.146813348	2455593.146877444	5.96×10^{-5}	9.01×10^{-7}	66
Ω (deg)	103.90116959022	103.90115152105	4.19×10^{-7}	3.61×10^{-9}	120
ω (deg)	149.98490769406	149.98494722851	5.03×10^{-7}	1.77×10^{-9}	280
i (deg)	7.13436678912	7.13436762265	4.83×10^{-8}	2.24×10^{-9}	22
a (AU)	2.361546969404	2.361546970577	2.12×10^{-9}	8.85×10^{-10}	2.4
P (days)	1325.541437127	1325.541438115	1.78×10^{-6}	7.46×10^{-7}	2.4
M (deg)	90.806023730	90.806006254	1.62×10^{-5}	2.96×10^{-7}	55

Please cite this article in press as: Konopliv, A.S., et al. The Vesta gravity field, spin pole and rotation period, landmark positions, and ephemeris from the Dawn tracking and optical data. Icarus (2013), http://dx.doi.org/10.1016/j.icarus.2013.09.005

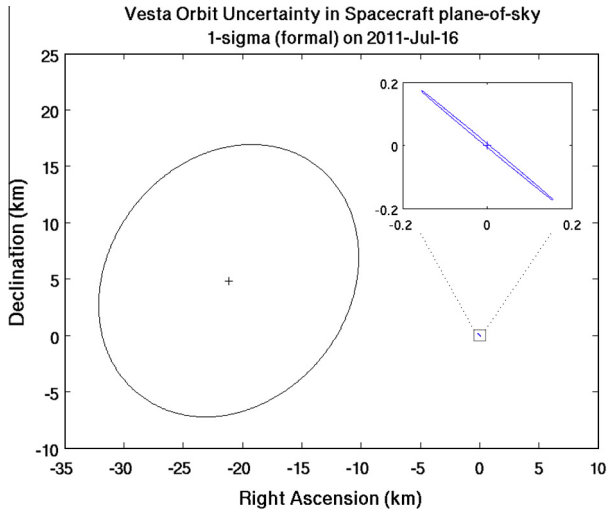

Fig. 19. Vesta orbit uncertainties projected on the Dawn spacecraft plane-of-sky near encounter (2011-July-16). The improvement in Vesta's orbit is apparent by comparing the relatively large uncertainty ellipse on the left (prior orbit) with the much reduced ellipse on the right (new orbit), which is also shown in the inset (upper right) magnified to show the scale and shape of the ellipse. The shift in the nominal position of Vesta (from prior orbit to new orbit) is about 2-sigma, which is likely due to unknown errors in pre-1950s data (a test of an orbit fit using only optical data from 1950 to 2012 moves the nominal position to less than one sigma from the new orbit's position).

Eunomia, 16 Psyche, 29 Amphitrite, 52 Europa, 65 Cybele, 87 Sylvia, 88 Thisbe, 511 Davida, and 704 Interamnia. The model also includes the effects of general relativity and solar corona effects on the X-band range data.

Although the orbit of Vesta prior to the Dawn encounter was well established, use of Dawn range data has substantially improved the orbit, reducing the uncertainties by two orders of magnitude for some orbital elements. A best-fit solution was obtained with corresponding osculating orbital elements and uncertainties shown in Table 7. Although the new orbit solution is largely dominated by the range data, the long time spanned by the optical astrometry (1827–2012, or about 50 orbits) contributes about a 30% improvement to Vesta's mean-motion, consistent with the small improvement to the uncertainties in semi-major axis (a) and orbital period (P). The uncertainty in orbital eccentricity has been reduced by two orders of magnitude (along with some of the angular elements) due to the very accurate, albeit indirect, measurement of Vesta's heliocentric range using the Dawn range data.

With this improved orbit, Vesta's position can be predicted to better than 100 km 150 years in the past and future, and better than 1 km around the time of the Dawn Vesta encounter. The improvement to Vesta's heliocentric orbit is shown by comparing ephemeris uncertainties in RTN coordinates between the prior orbit (Fig. 17) and the new orbit (Fig. 18). The RTN-frame is defined by a Sun–asteroid unit vector (R), a unit vector in the north direction normal to the asteroid's orbit plane (N), and by a transverse unit vector (T) that completes the right handed, orthogonal system such that $T = N \times R$. Figs. 17 and 18 show improvements of a factor of 8 in R, 2 in T, and 30 in N. The improvement to Vesta's orbit is also illustrated in Fig. 19, which shows the relative location of Vesta in the Dawn spacecraft plane-of-sky at encounter (2011-July-16) with corresponding uncertainty ellipses for both the prior orbit (large ellipse) and the new orbit (two orders of magnitude smaller).

The very accurate measurement of Vesta's position during the time of the Dawn encounter provides an opportunity to investigate unmodeled dynamics and/or biases in the optical data. A preliminary study of the effects of early optical data on the nominal orbit of Vesta at Dawn encounter, which showed a roughly 2-sigma difference between the prior Vesta orbit and the new orbit (Fig. 19), suggests that there are unmodeled biases in those early optical data. Optical-only orbits of Vesta computed ignoring data prior to 1950, 1970, and then 1980 show a movement in right ascension of the nominal orbit toward the new orbit's position. Further analysis may point to methods of correcting and/or de-weighting early optical data to improve orbits of other well observed main-belt asteroids.

Acknowledgments

Bill Owen modified the optical software to allow estimation of large landmark location data sets and modeling of asteroid precession and nutation. We thank the Dawn Navigation team (in particular Nick Mastrodemos, Don Han, and Brian Kennedy) for many helpful discussions and modeling information. The research described in this paper was carried out at the Jet Propulsion Laboratory, California Institute of Technology, under contract with the National Aeronautics and Space Administration.

References

Archinal, B.A. et al., 2011. Report of the IAU working group on cartographic coordinates and rotational elements: 2009. Celest. Mech. Dynam. Astron. 109, 101–135.

Asmar, S.W., Armstrong, J.W., Iess, L., Tortora, P., 2005. Spacecraft Doppler tracking: Noise budget and achievable accuracy in precision radio science observations. Radio Sci. 40, RS2001. http://dx.doi.org/10.1029/2004RS003101.

Baer, J., Milani, A., Chesley, S.R., Matson, R.D., 2008. An observational error model, and application to asteroid mass determination. Bull. Am. Astron. Soc. 40, 493.

Bierman, G.J., 1977. Factorization Methods for Discrete Sequential Estimation. Academic Press, New York.

Bills, B.G., Asmar, S.W., Konopliv, A.S., Park, R.S., Raymond, C.A., 2013. Harmonic and statistical analyses of the gravity and topography of Vesta. Icarus, submitted for publication.

Chesley, S.R., Baer, J., Monet, D.G., 2010. Treatment of star catalog biases in asteroid astrometric observations. Icarus 210, 158–181.

Delsate, N., 2012. Analytical and numerical study of the ground-track resonances of Dawn orbiting Vesta. Planet. Space Sci. 59 (13), 1372–1383.

Drummond, J., Eckhart, A., Hege, E.K., 1988. Speckle interferometry of asteroids. IV. Reconstructed images of 4 Vesta. Icarus 73, 1–14.

Ermakov, A.I., Zuber, M.T., Smith, D.E., Raymond, C.A., Balmino, G., Fu, R.R., Ivanov, B.A., 2013. Modeling of Vesta's interior structure using gravity and shape models form the Dawn mission. Icarus, submitted for publication.

Fienga, A. et al., 2009. INPOP08, a 4-D planetary ephemeris: From asteroid and time-scale computations to ESA Mars Express and Venus Express contributions. Astron. Astrophys. 507 (3), 1675–1686. http://dx.doi.org/10.1051/0004-6361/200911755.

Folkner, W.M., 2010. Mars Ephemeris Uncertainty for Mars Science Laboratory Navigation. JPL Internal Document 343R-10-001. Jet Propulsion Laboratory, Pasadena, CA.

Folkner, W.M. et al., 1994. Determination of the extragalactic-planetary frame tie from joint analysis of radio interferometric and lunar laser ranging measurements. Astron. Astrophys. 287, 279–289.

Garmier, R., Barriot, J.P., 2001. Ellipsoidal harmonic expansions of the gravitational potential: Theory and application. Celest. Mech. Dynam. Astron. 79, 235–275.

Garmier, R., Barriot, J.P., Konopliv, A.S., Yeomans, D.K., 2002. Modeling of the Eros gravity field as an ellipsoidal harmonic expansion from the NEAR Doppler tracking data. Geophys. Res. Lett. 29. http://dx.doi.org/10.1029/2001GL013768.

Gaskell, R.W. et al., 2008. Characterizing and navigating small bodies with imaging data. Meteorit. Planet. Sci. 43, 1049–1061.

Grafarend, E., Engels, J., 1994. The convergent series expansion of the gravity field of a starshaped body. Manuscr. Geodaet. 19, 18–30.

Heiskanen, W.A., Moritz, H., 1967. Physical Geodesy. W.H. Freeman and Company, San Francisco and London.

Jaumann, R. et al., 2012. Vesta's shape and morphology. Science 336 (6082), 687–690. http://dx.doi.org/10.1126/science.1219122.

Kaula, W.M., 1963. The investigation of the gravitational fields of the Moon and planets with artificial satellites. Adv. Space Sci. Technol. 5, 210–230.

Kaula, W.M., 1966. Theory of Satellite Geodesy. Blaisdell, Waltham, MA.

Konopliv, A.S., Miller, J.K., Owen, W.M., Yeomans, D.K., Giorgini, J.D., Garmier, R., Barriot, J.P., 2002. A global solution for the gravity field, rotation, landmarks, and ephemeris of Eros. Icarus 160, 289–299.

Konopliv, A.S., Yoder, C.F., Standish, E.M., Yuan, D.N., Sjogren, W.L., 2006. A global solution for the Mars static and seasonal gravity, Mars orientation, Phobos and Deimos masses, and Mars ephemeris. Icarus 182, 23–50.

Konopliv, A.S. et al., 2011a. The Dawn gravity investigation at Vesta and Ceres. Space Sci. Rev. 163, 461–486. http://dx.doi.org/10.1007/s11214-011-9794-8.

Konopliv, A.S., Asmar, S.W., Folkner, W.M., Karatekin, O., Nunes, D.C., Smrekar, S.E., Yoder, C.F., Zuber, M.T., 2011b. Mars high resolution gravity fields from MRO, Mars seasonal gravity, and other dynamical parameters. Icarus 211, 401–428.

Krening, S.C., Semenov, B.V., Acton, C.H., 2012. Dawn Spice Kernels V1.0, Dawn-M/A-Spice-6-V1.0. NASA Planetary Data System.

Krogh, F.T., 1973. Changing Stepsize in the Integration of Differential Equations using Modified Divided Differences, JPL Technical Memorandum No. 312, Section 914 (Internal Document). Jet Propulsion Laboratory, California Institute of Technology, Pasadena, CA.

Kuchynka, P., Folkner, W.M., 2013. A new approach to determining asteroid masses from planetary range measurements. Icarus 222, 243–253.

Kuzmanoski, M., Apostolovska, G., Novaković, B., 2010. The mass of (4) Vesta derived from its largest gravitational effects. Astron. J. 140 (3), 880–886. http://dx.doi.org/10.1088/0004-6256/140/3/880.

Lambeck, K., 1988. Geophysical Geodesy. Clarendon Press, Oxford.

Lawson, C.L., Hanson, R.J., 1995. Solving Least Squares Problems. SIAM Classics in Applied Mathematics, vol. 15. Society for Industrial and Applied Mathematics, Philadelphia.

Li, J.-Y., Thomas, P.C., Carcich, B., Mutchler, M.J., McFadden, L.A., Russell, C.T., Weinstein-Weiss, S.S., Rayman, M.D., Raymond, C.A., 2010. Improved measurement of Asteroid (4) Vesta's rotational axis orientation. Icarus 211, 528–534.

Mandler, B.E., Elkins-Tanton, L.T., 2013. The origin of eucrites, diogenites, and olivine diogenites: Magma ocean crystallization and shallow magma chamber processes on Vesta. Meteorit. Planet. Sci., 1–17. http://dx.doi.org/10.1111/maps.12135.

McSween Jr., H.Y., Mittlefehldt, D.W., Beck, A.W., Mayne, R.G., McCoy, T.J., 2011. HED meteorites and their relationship to the geology of Vesta and the Dawn mission. Space Sci. Rev. 163, 141–174. http://dx.doi.org/10.1007/s11214-010-9637-z.

McSween, H.Y. et al., 2013. Composition of the Rheasilvia basin: A window into Vesta's interior. J. Geophys. Res. 118, 335–346. http://dx.doi.org/10.1002/jgre.20057.

Michalak, G., 2000. Determination of asteroid masses – I. (1) Ceres, (2) Pallas, and (4) Vesta. Astron. Astrophys. 360, 363–374.

Moyer, T.D., 1971. Mathematical Formulation of the Double-precision Orbit Determination Program (DPODP). JPL Technical Report 32-1527. Jet Propulsion Laboratory, California Institute of Technology, Pasadena, CA.

Moyer, T.D., 2000. Formulation for Observed and Computed Values of Deep Space Network Data Types for Navigation, Monograph 2 of Deep Space Communications and Navigation Series, JPL Publication 00-7. Jet Propulsion Laboratory, California Institute of Technology, Pasadena, CA.

Muller, P.M., Sjogren, W.L., 1968. Mascons: Lunar Mass Concentrations. Science 161, 680–684.

Owen Jr., W.M., Wang, T.C., Harch, A., Bell, M., Peterson, C., 2001. NEAR optical navigation at Eros. AAS Paper 01-376, Presented at AAS/AIAA Astrodynamics Specialists Conference, Quebec City, Quebec, Canada.

Park, R.S., Konopliv, A.S., Asmar, S.W., Bills, B.G., Gaskell, R., Raymond, C.A., Smith, D.E., Toplis, M.J., Zuber, M.T., 2013. Gravity field expansion in ellipsoidal harmonics and alternate internal representations applied to Vesta. Icarus, submitted for publication.

Pitjeva, E.V., 2005. High-precision ephemerides of planets – EPM and determination of some astronomical constants. Solar Syst. Res. 39, 176–186.

Rambaux, N., 2013. The rotational motion of Vesta. Astron. Astrophys.. http://dx.doi.org/10.1051/0004-6361/201220732, 556, A151.

Raymond, C.A. et al., 2011. The Dawn topography investigation. Space Sci. Rev. 163, 487–510. http://dx.doi.org/10.1007/s11214-011-9863-8.

Russell, C.T. et al., 2012. Dawn at Vesta: Testing the protoplanetary paradigm. Science 336 (6082), 684–686. http://dx.doi.org/10.1126/science.1219381.

Ruzicka, A., Snyder, G.A., Taylor, L.A., 1997. Vesta as the howardite, eucrite and diogenite parent body: Implications for the size of a core and for large-scale differentiation. Meteorit. Planet. Sci. 32, 825–840.

Standish, E.M., 2001. Suggested GM Values for Ceres, Pallas, and Vesta. JPL Interoffice Memorandum (Internal Document), 312.F-01-006, April 11, 2001.

Tapley, B.D., Schutz, B.E., Born, G.H., 2004. Statistical Orbit Determination. Elsevier, Boston.

Thomas, P.C., Binzel, R.P., Gaffey, M.J., Zellner, B.H., Storrs, A.D., Wells, E., 1997. Vesta: Spin pole, size, and shape from HST images. Icarus 128, 88–94.

Thomas, V.C. et al., 2011. The Dawn spacecraft. Space Sci. Rev. 163, 175–249. http://dx.doi.org/10.1007/s11214-011-9852-2.

Tricarico, P., Sykes, M.V., 2010. The dynamical environment of Dawn at Vesta. Planet. Space Sci. 58, 1516–1525.

Ward, W.R., Hamilton, D.P., 2004. Tilting Saturn. I. Analytic model. Astron. J. 128, 2501–2509.

Yeomans, D.K., Chodas, P.W., Keesey, M.S., Ostro, S.J., Chandler, J.F., Shapiro, I.I., 1992. Asteroid and comet orbits using radar data. Astron. J. 103, 303–317.

Zuber, M.T. et al., 2011. Origin, internal structure and evolution of 4 Vesta. Space Sci. Rev. 163, 77–93. http://dx.doi.org/10.1007/s11214-011-9806-8.

Please cite this article in press as: Konopliv, A.S., et al. The Vesta gravity field, spin pole and rotation period, landmark positions, and ephemeris from the Dawn tracking and optical data. Icarus (2013), http://dx.doi.org/10.1016/j.icarus.2013.09.005